Fingerprinting the nonlinear rheology of a liquid crystalline polyelectrolyte

Ryan J. Fox, Wei-Ren Chen, Changwoo Do, Stephen J. Picken, M. Gregory Forest & Theo J. Dingemans

Rheologica Acta

ISSN 0035-4511
Volume 59
Number 10

Rheol Acta (2020) 59:727-743
DOI 10.1007/s00397-020-01234-4

Springer

Rheologica Acta (2020) 59:727–743
https://doi.org/10.1007/s00397-020-01234-4

ORIGINAL CONTRIBUTION

Fingerprinting the nonlinear rheology of a liquid crystalline polyelectrolyte

Ryan J. Fox[1] · Wei-Ren Chen[2] · Changwoo Do[2] · Stephen J. Picken[3] · M. Gregory Forest[1,4] · Theo J. Dingemans[1]

Received: 18 May 2020 / Revised: 28 July 2020 / Accepted: 3 August 2020 / Published online: 25 August 2020

Abstract

We report on the rheology of isotropic and nematic aqueous solutions of a sulfonated all-aromatic polyamide, poly(2,2′-disulfonyl-4,4′-benzidine terephthalamide) (PBDT), that forms high-aspect-ratio rod-like assemblies. For quiescently isotropic solutions, the concentration dependence of the zero-shear viscosity, longest relaxation time, and terminal modulus shows deviations in comparison to the Doi-Edwards theory for hard rods. For quiescently nematic solutions, we characterize the flow behavior through steady-state and transient nonlinear rheological measurements in conjunction with small-angle neutron scattering under shear. The steady-state flow curve is characterized by two anomalous shear thickening responses, one at moderate shear rates and the other immediately prior to flow alignment at high shear rates. We assign the origin of these shear thickening response to director "kayaking" and "out-of-plane steady" states, using predictions from prior high-resolution numerical simulations of sheared nematic rods. Utilizing transient shear flow reversals and step-down experiments, we characterize the oscillatory response of the nematic director through these flow regimes. When the first normal stress difference is plotted versus the shear stress during a transient step-down, the so-called dynamic stress path, the counterclockwise versus clockwise rotation has previously been shown to reveal the relative dominance of viscous versus elastic contributions to the stress tensor, respectively. Our measurements strongly suggest that the anomalous shear thickening behavior in nematic PBDT solutions arises from viscous stresses developed as the ensemble of rods undergoes periodic oscillatory motion under shear, rather than elastic stresses due to broadening of the orientational distribution function.

Keywords Nonlinear rheology · Liquid crystal polymer · Polyelectrolyte · Small-angle neutron scattering · Rheo-SANS

Introduction

All-aromatic polyamides (aramids) are a class of rigid, thermally stable polymers, most notably poly(*p*-phenylene terephthalamide) (PPTA), used commercially in the production of high-strength fibers (Picken 1992). When dissolved in 100% H_2SO_4 above a critical concentration, PPTA rod-like polymers spontaneously align into a liquid crystalline (nematic) phase due to an anisotropic intermolecular potential (Picken 1989). Within each monodomain of defect-free nematic order, there is a unique peak in the orientational distribution of the rod-like molecules, called the nematic director (Doi and Edwards 1986). On mesoscopic length scales in the quiescent state, nematic monodomains are separated by disclinations (topological defects), resulting in an isotropic distribution when averaged over all local monodomain directors, giving rise to the classic Schlieren polydomain texture (Gennes and Prost 1978). The shear flow behavior of nematic liquid crystalline polymers (LCPs) in general is exceedingly

Electronic supplementary material The online version of this article (https://doi.org/10.1007/s00397-020-01234-4) contains supplementary material, which is available to authorized users.

✉ M. Gregory Forest
forest@unc.edu

✉ Theo J. Dingemans
tjd@unc.edu

[1] Department of Applied Physical Sciences, University of North Carolina at Chapel Hill, Chapel Hill, NC 27599-3050, USA

[2] Neutron Scattering Division, Oak Ridge National Laboratory, Oak Ridge, TN 37831, USA

[3] Faculty of Applied Sciences, Delft University of Technology, Van der Maasweg 9, 2629 HZ Delft, The Netherlands

[4] Department of Mathematics, University of North Carolina at Chapel Hill, Chapel Hill, NC 27599-3250, USA

complex and only partially understood (Burghardt 1998, Noel and Navard 1991, Wissbrun 1981). Complexities arise, in part, from the transient response of individual monodomains and the collective polydomain structure that manifests under imposed shear (Wissbrun 1981; Doi and Edwards 1986; Marrucci 1985). From both a technological and scientific perspective, it is important to further investigate the rheological behavior of LCPs of specific interest and to connect their bulk rheology to the transient behavior of sheared nematic monodomains.

Unlike PPTA, where dissolution requires strong mineral acids, sulfonated derivatives of aramids (sulfo-aramids) can be dissolved into water (Funaki et al. 2004; Gao et al. 2015; Sarkar and Kershner 1996; Viale et al. 2004a, 2005). A variety of sulfo-aramids are known to form high-aspect-ratio supramolecular assemblies in aqueous solution, resulting in the formation of liquid crystalline phases at relatively low concentrations (~ 1–2 wt%). The liquid crystallinity and water solubility of sulfo-aramids enable fabrication of solid-state membranes with anisotropic morphologies and structures via environmentally benign processing conditions. As a result, sulfo-aramids have been investigated for use in proton exchange membranes for fuel cells (Every et al. 2006a, 2006b), matrices for solid-state battery electrolytes incorporating ionic liquids (Bostwick et al. 2020, Fox et al. 2019, Wang et al. 2016, Yu et al. 2017), water transport membranes (Gao et al. 2015), dual-network hydrogels (Wu et al. 2010), hybrid biaxial liquid crystalline nanocomposites (Hegde et al. 2020), and as novel rheopectic materials that can undergo a liquid-to-solid transition due to irreversible, shear-activated gelation (Fox et al. 2020b).

While it can be expected that the rheological behavior of these liquid crystalline sulfo-aramid solutions is similar to other lyotropic LCPs, the details have not been extensively investigated. Viale et al. reported small-angle neutron scattering spectra under shear (rheo-SANS) on a 1 wt% solution of sulfo-PPTA in water with Li^+ counterions (Viale et al. 2004b). Strongly anisotropic scattering patterns were observed under shear, indicating a high degree of molecular alignment. The 1–3 plane (flow-vorticity plane) apparent order parameter, which is unity for perfect orientation and zero in the isotropic case (Picken et al. 1990), increased from 0.3 at a shear rate of 25 s^{-1} to 0.55 at 2500 s^{-1}. Upon flow cessation, the relaxation of shear-induced orientation was extraordinarily slow and attributed to the presence of high-aspect-ratio needle-like aggregates. However, measurements of basic rheological properties, such as the viscosity and first normal stress difference in steady and transient flows, and their correlation to observed scattering anisotropy, have not been reported for lyotropic sulfo-aramids.

Herein, the sulfo-aramid that we investigate is poly(2,2′-disulfonyl-4,4′-benzidine terephthalamide) (PBDT) with Na^+ counterions. Fully nematic solutions of PBDT can be obtained at solution concentrations of ~ 2 wt% in water (Gao et al. 2015; Wang et al. 2014, 2016). Recently, we reported on the steady-state and transient nonlinear rheology of PBDT solutions in water (Fox et al. 2020a). We found that PBDT exhibits some rheological behaviors that are prototypical for LCPs in the nematic phase, such as a regime of negative first normal stress difference (N_1), and hesitation of the viscosity prior to shear thinning at high shear rate (Kiss and Porter 1978, 1980; Marrucci and Maffettone 1989). However, the negative N_1 regime occurred over an extremely narrow shear rate range, unlike the widely studied model LCPs, poly(benzyl glutamate) (PBG) in *m*-cresol (Kiss and Porter 1978, 1980; Maffettone et al. 1994; Mewis et al. 1997; Moldenaers and Mewis 1986) and hydroxypropyl cellulose (HPC) in water (Grizzuti et al. 1990; Moldenaers et al. 1994) or *m*-cresol (Baek et al. 1993a; Baek et al. 1994). In addition, we also observed anomalous shear thickening in the steady-state flow curves and regimes of strongly oscillating stress transients following shear step-down from the flow-aligned state. We suggested that the behavior of nematic PBDT solutions under shear is distinct from the oscillating stresses previously reported by Mewis et al. (Mewis et al. 1997) on PBG in *m*-cresol and found by Lettinga et al. (Lettinga and Dhont 2004; Lettinga et al. 2005) on *fd* virus suspensions, attributed by both of these authors to wagging (finite oscillations of the nematic director within the plane of shear). This wagging state was originally believed to separate low shear rate director tumbling (continuous rotation in the shear plane) and high shear rate director alignment at some angle in the shear plane. Using previous extensive, high-resolution, numerical simulations by Forest et al. (Forest et al. 2004a, b), we instead inferred that the origin of anomalous shear thickening of nematic PBDT arises from director kayaking—marked by periodic rotation of the director around the vorticity axis, akin to the oars of a kayaker.

Outline of presentation and results for the present paper We report measurements of the nonlinear rheological properties of PBDT in D_2O, spanning the isotropic and fully nematic concentration regimes. The zero-shear viscosity, relaxation time, and terminal modulus are determined as a function of concentration and compared to the predictions of the Doi-Edwards theory for rigid rods (Doi 1981, Doi and Edwards 1978b, Doi and Edwards, 1978a, Doi and Edwards 1986). Quiescently isotropic solutions exhibit anomalous, non-monotonic behavior in the first normal stress difference N_1. In the quiescent, fully nematic phase, the steady-state flow curves exhibit an unusual shape that features two distinct regimes of shear thickening. We investigate these flow regimes using transient rheological measurements (flow reversals and shear step-downs) and steady-state rheo-small-angle neutron scattering (rheo-SANS) measurements. A hesitation in the flow curve is concomitant with the onset of a negative first normal stress difference N_1 together with strongly oscillating stress transients,

as observed in other lyotropic systems (Grosso et al. 2003; Lettinga and Dhont 2004; Lettinga et al. 2005; Mewis et al. 1997). We find a narrow shear rate regime of weak shear thickening immediately prior to flow alignment, which does not exhibit oscillating stress transients, providing potential evidence for the out-of-plane steady director state found in numerical simulations (Forest et al. 2004a). Finally, using transient shear step-down experiments, we construct so-called dynamic stress paths (i.e., the first normal stress difference versus the shear stress) whose rotational chirality indicates the relative importance of elastic and viscous stresses (Maffettone et al. 1994; Moldenaers et al. 1994). We find that the shear thickening behavior is associated with dominance of the viscous stress contribution, supporting kayaking as the responsible director response state. Our results provide new insights into the flow behavior of nematic LCPs that are not dominated by the elasticity of the polydomain defect texture.

Materials and methods

Materials The polymer sample used here is the same as that in our previous publication (Fox et al. 2020a). The nematic solutions were prepared by mixing PBDT and deuterium oxide (D_2O) and heating at 60 °C for at least 1 week with magnetic stirring. Polymer solutions exhibited fully nematic phase behavior at concentrations at 19 g L^{-1} and above in D_2O, consistent with our prior study.

Rheology For all rheological measurements presented, we employed a stress-controlled Anton Paar MCR 302 rheometer operating in strain-controlled mode with a 50-mm $\beta = 0.982°$ cone and plate geometry. The temperature was controlled at 25 ± 0.01 °C by a circulating water bath under the bottom stationary plate. A low viscosity oil bath around the sample edges prevented evaporation that enabled sample stability over long time periods. All samples were pre-sheared for several thousand strain units at the highest shear rate investigated for each individual flow curve. This procedure erased of the sample's shear history and provided a consistent starting point for each concentration from which to construct the steady-state flow curves and measure stress transients. The calculated N_1 values were corrected for inertia by using $N_1 = [2F_z/(\pi R^2)] + [(3\pi\rho\omega^2 R^4)/40]$, where $\omega = \beta\dot{\gamma}$ is the angular rotation rate (Kulicke et al. 1977). The baseline in N_1 was determined by taking the average of the instrumental background for 100 s before and after measurement at each discrete shear rate. During steady shear, N_1 was averaged over at least 500 strain units at steady state, and up to 2500 strain units for small values of N_1, after decay of the initial stress transient.

Rheo-SANS Rheo-SANS measurements were performed at the Extended Q-Range Small-Angle Neutron Scattering Diffractometer (EQ-SANS) at the Spallation Neutron Source (SNS) at Oak Ridge National Laboratory (ORNL). One configuration was used, with a sample-to-detector distance of 1.3 m with an incident neutron wavelength of 8 Å, which provided data over a q-range of 0.05 to 0.3 $Å^{-1}$. An Anton Paar MCR 502 was utilized with a 49-mm concentric cylinder geometry. The liquid crystalline solutions were poured into the outer quartz cell, and the Ti inner cylinder was lowered into position. Solvent evaporation was prevented by an oil-sealed solvent trap, which saturated the sample headspace with solvent vapor. The shear gap was 1 mm; thus, the total sample path length was 2 mm. All scattering measurements were corrected for detector background, sensitivity, empty cell scattering, and sample transmission using standard methods at the EQSANS beamline in MantidPlot. Scattering data was converted to absolute units using a calibrated standard. The 2D scattered intensity was azimuthally integrated using the Nika package for Igor Pro 8 (Ilavsky 2012), and fit with the Maier-Saupe orientational distribution function to calculate the 1–3 plane apparent order parameter (Picken et al. 1990).

Results and discussion

Nonlinear rheology in the isotropic phase

We plot the steady-state viscosity as a function of shear rate for quiescently isotropic PBDT solutions in Fig. 1. The qualitative shape of the flow curves is typical of isotropic polymeric solutions, exhibiting a zero-shear viscosity plateau and shear thinning at shear rates greater than a critical shear rate. In the isotropic state, the critical shear rate for the onset of shear thinning corresponds to the inverse of the longest relaxation time of the constituent particles. For dilute rod-like particles in the isotropic phase, the longest relaxation time is the rotational diffusivity, given by $D_r^0 = k_B T/\zeta_{str} = 3k_B T[\ln(L/D) - 0.8] / (\pi\eta_s L^3)$ where $k_B T$ is the thermal energy, ζ_{str} is the rod-solvent friction coefficient, L and D are the length and diameter of the rod, and η_s is the solvent viscosity (Doi and Edwards 1986). Taking L = 373 nm, D = 0.8 nm, and $\eta_s = 0.89 \times 10^{-3}$ Pa s, we calculate $D_r^0 = 455\ s^{-1}$, yielding a relaxation time of $\tau = 1/(2D_r^0) = 1.1 \times 10^{-3}$ s, and an approximate critical shear rate $\dot{\gamma}_c \approx 1/\tau \approx 910\ s^{-1}$. The calculated critical shear rate is in good agreement with the onset of shear thinning at the lowest concentrations studied here.

As the solution concentration is increased, the onset of shear thinning shifts to lower shear rates and the relative magnitude of viscosity shear thinning increases. For polymer solutions in general, shear thinning originates from shear-induced alignment along the elongational component of the

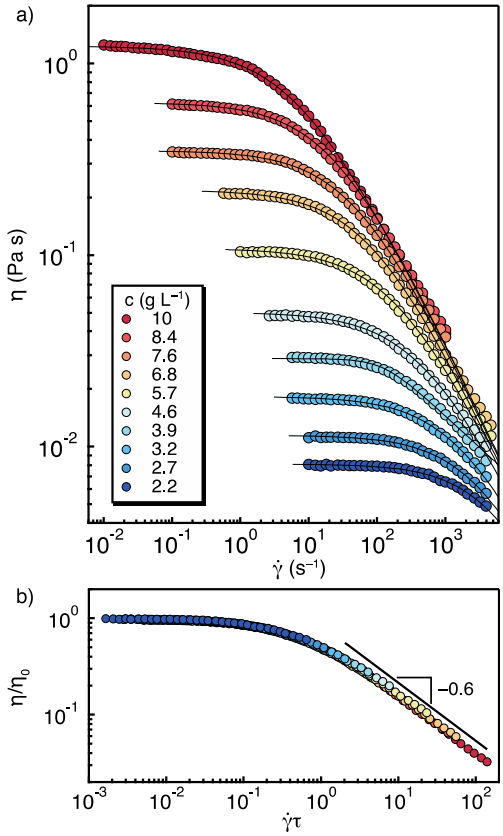

Fig. 1 **a** Steady-state viscosity as a function of shear rate for quiescently isotropic PBDT solutions in D_2O. Solid lines are fits to the Cross model. **b** Normalized viscosity versus rescaled shear rate obtained from fitting the flow curves

shear field. Compared to flexible polyelectrolytes, such as poly(2-vinylpyridine) (PVP) at similar solution viscosities (Dou and Colby 2008), the observed shear thinning is more dramatic for isotropic PBDT solutions. For example, PVP in NMF with a zero-shear viscosity of ~ 1 Pa s decreases by a factor of 2 as the shear rate is increased by a factor of 400, whereas the viscosity of a 10 g L^{-1} PBDT solution decreases by a factor of 50 over the same shear rate range. This is likely due to the large aspect ratio of the PBDT rod-like particles and strong orientational effect of the shear flow. To extract the zero-shear viscosity and longest relaxation time for the isotropic PBDT solutions, we fit the data with the empirical Cross model

$$\eta = \eta_\infty + \frac{\eta_0 - \eta_\infty}{1 + \left(\tau\dot{\gamma}\right)^m}$$

where η_∞ and η_0 are the infinite- and zero-shear viscosity, respectively, τ is the longest relaxation time, and m is the shear thinning exponent. We set η_∞ to 0 while fitting the flow curves, as we did not observe an onset of an infinite-rate plateau viscosity. The Cross-model fits to the steady-state flow curves are shown as the solid lines in Fig. 1(a). We also attempted to fit the steady-state flow curve with the Carreau model; however, the model could not capture the qualitative shape of the flow curve satisfactorily. While both models fit the data well at low shear rates and deviate at high shear rates, shown in Fig. S1, the Carreau model exhibits a much sharper transition at the critical shear rate when compared to the Cross model. This is in contrast to the data of Lang et al. on isotropic suspensions of rod-like *fd* virus, who found good agreement with the Carreau model (Lang et al. 2019). The differences between PBDT and *fd* virus suspensions, and discrepancy between the two model fits, may originate from the polydispersity of PBDT rods that results in a distribution of relaxation times. In contrast, *fd* virus suspensions are monodisperse and the longest relaxation time is well-defined (Lettinga and Dhont 2004). However, the strong shear thinning that both systems exhibit originate from the development of a highly aligned shear-induced paranematic state (Lang et al. 2019; Lettinga and Dhont 2004).

Through fitting the flow curves with the Cross model, we normalize the viscosity to the zero-shear viscosity and rescale the shear rate by the longest relaxation time and were able to collapse the data into a single mastercurve, plotted in Fig. 1(b). The collapse of the data shows that the flow behavior of isotropic PBDT solutions are well-described by these two parameters. We observe a common shear thinning exponent for all concentrations at high shear rates, shown by the power law with slope − 0.6 in the figure. This value is similar to the shear thinning power laws found for fully nematic PBDT solutions at high shear rates (see below), consistent with enhanced orientation of the rods under shear.

The zero-shear viscosity obtained from the flow curve fitting is plotted in Fig. 2(a) as a function of concentration. The maximum in the zero-shear viscosity approximates the I-N transition concentration above which the isotropic phase is unstable to incipient nematic ordering (Doi and Edwards 1986). Below this concentration, we find three distinct regimes of power law scaling of the zero-shear viscosity that correspond to the dilute, semidilute, and concentrated isotropic regimes, respectively, indicated by breaks in the power law fits to the data. For further detail on the predicted power laws for the rheological properties of rigid-rod polymers in solution, we direct the reader to Doi and Edwards (Doi and Edwards 1986).

For rigid rods in a dilute, isotropic solution, η_0 is predicted to increase linearly with concentration, found here below ~ 2.7 g L^{-1}. In the semidilute concentration regime, the predicted and experimentally found scaling relationship for η_0 versus concentration and molecular weight (i.e., length) in the semidilute isotropic regime is 3 and 6, exhibiting a strong entanglement effect (Baird and Ballman 1979; Doi 1981). Here, we find that the scaling relationship $\eta_0 \sim c^3$ is consistent with these predictions in the semidilute isotropic regime. At

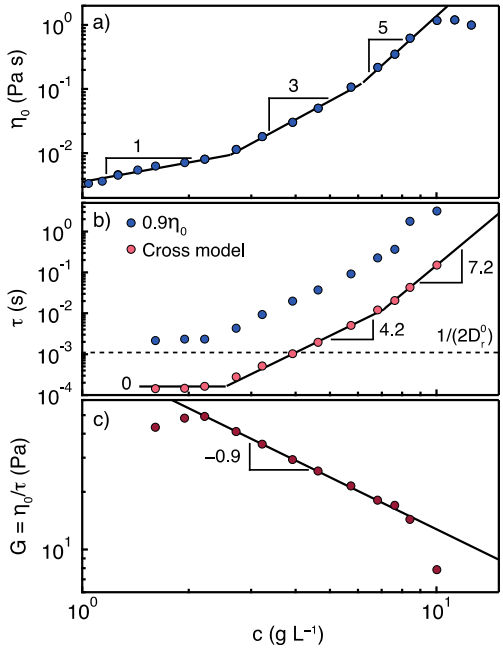

Fig. 2 Results of fitting steady-state viscosity flow curves with the Cross model: (a) zero-shear viscosity, (b) terminal relaxation time, and (c) terminal modulus. Power law exponents are given in the figure

higher concentrations, the viscosity scaling increases to $\eta_0 \sim c^5$, which is not predicted by the Doi-Edwards theory, but has been suggested to arise from rod-jamming effects (Doi and Edwards 1986).

The τ obtained by fitting the flow curve with the Cross model is plotted in Fig. 2(b) as a function of concentration. In addition, we estimated τ in a model-independent fashion by taking the inverse of the shear rate when the steady-state viscosity reaches 90% of the zero-shear viscosity (Lopez et al. 2015); see Fig. S1. Fitting the Cross model to the data gave relaxation times smaller than the model-free procedure by about a factor of 20, but both methods gave the same concentration scaling laws, giving confidence to the reported power law exponents and trends of the data.

Below ~2 g L^{-1}, the experimentally determined τ remains constant, consistent with dilute solution conditions. We calculated τ for rods in dilute solution, given as $\tau \approx 1/(2D_r)$, using the known diameter (Wang et al. 2014, 2019) and estimated length of PBDT rods of 373 nm (based on the application of the Onsager theory for hard rods to the isotropic-nematic (I-N) transition concentration we find here (Vroege and Lekkerkerker 1992)), shown as the horizontal dashed line in Fig. 2(b). The calculated relaxation time is in approximate agreement with the relaxation time found from the model-free fitting procedure.

In the semidilute regime, we find $\tau \sim c^{4.2}$, whereas the Doi-Edwards model predicts a quadratic dependence, showing a much stronger entanglement effect on the rotational dynamics. We do not ascribe this deviation to an exact cause, but surmise the potential effect of finite stiffness in the experimental system, possibly leading to the presence of hairpin defects (Picken et al. 1998), or the presence of transient hydrophobic interactions (Lopez et al. 2018) that may contribute to the stronger concentration dependence of the relaxation time. At the crossover from semidilute to the concentrated isotropic solution regime at 6.8 g L^{-1}, we find a strong power law scaling $\tau \sim c^{7.2}$ until the I-N transition concentration at ~ 11 g L^{-1}. As the concentration approaches the I-N transition, the relaxation time is expected to diverge, although this is never experimentally observed due to phase separation into an anisotropic phase (Doi and Edwards 1986). Overall, these data evidence a significant slowing down of the rod dynamics under shear as the solution concentration is increased throughout the isotropic regime.

We estimated the solution terminal modulus $G = \eta_0/\tau$, using τ obtained from the Cross model fitting, and plot G as a function of concentration in Fig. 2(c). This method is known to accurately estimate G that would be found from linear viscoelastic measurements for salt-free polyelectrolyte solutions (Dou and Colby 2006). For semidilute, unentangled polyelectrolyte solutions, G is predicted to scale linearly with concentration with a contribution of k_BT per chain (Dobrynin et al. 1995). Here, below a concentration of ~ 2.2 g L^{-1}, G appears to be increasing before reaching a maximum (although the limited data makes this conclusion uncertain), then decreases with concentration following a power law of − 0.9. At 10 g L^{-1}, G suddenly decreases and appears to diverge towards zero. This behavior arises from the stronger concentration dependence of τ in comparison to η_0. That is, the dynamics of rod rearrangement under shear slows down more strongly than the viscosity increases. We speculate that pretransitional effects result in an increase in local orientational order, without formation of a nematic phase, and leads to the observed decrease in G (Doi and Edwards 1986). The presence of pretransitional effects prior to the I-N phase separation is further supported by anomalous, non-monotonic behavior of N_1 of quiescently isotropic solutions under shear, see Fig. S2.

To compare the terminal modulus obtained from the nonlinear rheology measurements to the moduli obtained from linear oscillatory measurements, we measured the frequency dependence of G' and G'' in the linear viscoelastic regime for solutions between 4.6 and 10 g L^{-1}, given in Fig. S3, and find a liquid-like response ($G'' > G'$). The limiting slopes at low frequencies are $G'' \sim \omega^1$ and $G' \sim \omega^{1.5}$, in contrast to the predicted scaling of terminal flow of $G'' \sim \omega^1$ and $G' \sim \omega^2$. Deviations from terminal flow frequency scaling of G' and G'' are well-known to occur in concentrated solutions of isotropic rod-like polymers (Kiss and Porter 1978). We plot G' evaluated at 10 rad s^{-1} in Figure S4, and find a strong concentration dependence scaling as $G' \sim c^{5.8}$. The differences observed between the linear oscillatory measurements and nonlinear rheology are consistent with strong orientational effects under nonlinear shear.

Nonlinear rheology in the nematic phase

At solution concentrations of 19 g L^{-1} and above, we observe fully liquid crystalline phase behavior as observed via polarized optical microscopy. We investigated the nonlinear rheology of the nematic solutions slightly above the fully nematic concentration to reduce the elastic contribution to the shear stress arising from domain distortion. In Fig. 3, we plot the steady-state η (*top*) and N_1 (*bottom*) as a function of shear rate for solution concentrations of 21, 23, and 30 g L^{-1}.

The flow curves of the nematic solutions are qualitatively different than the quiescently isotropic PBDT solutions, shown previously in Fig. 1. Overall, we observe a complex dependence of the viscosity on the shear rate, including both shear thinning and shear thickening over various ranges of the applied shear rate, and must describe the observed behavior in a stepwise fashion in the following discussion. A zero-shear viscosity plateau is not clearly present, as is the case in the isotropic phase of PBDT. Although the observed shear thinning at low shear rates is quite weak, it is clearly present when a direct comparison is made to isotropic solutions of similar viscosity. Due to the low torque signal at low shear rates and large strains required to reach steady state, we did not investigate lower shear rates to determine if a Newtonian plateau region was present.

In general, the flow curves of LCPs are described by a three flow curve model given by Onogi and Asada (Onogi and Asada 1980), with shear thinning at low and high shear rates (regions I and III) separated by a pseudo-Newtonian plateau at moderate shear rates (region II). For PBG, the region II plateau and region III shear thinning regimes are generally observed over the experimentally accessible shear rate regime, but region I shear thinning is not observed (Kiss and Porter 1978, 1980; Moldenaers and Mewis 1986). Region I shear thinning is generally characterized by a low degree of shear-induced alignment and a shear thinning power law of − 0.5 at low shear rates (Hongladarom and Burghardt 1998; Ugaz and Burghardt 1997; Walker et al. 1997; Walker et al. 1995). Based on the lack of a plateau viscosity at the lowest shear rates studied here, and absence of strong shear thinning behavior, we suggest that the entire flow curve for the liquid crystalline PBDT solutions studied here is likely within region III. This is likely due to the high axial rigidity of PBDT rods (> 400), in comparison to molecular liquid crystalline polymer solutions that possess lower persistence lengths, making PBDT rods strongly influenced by an imposed shear flow.

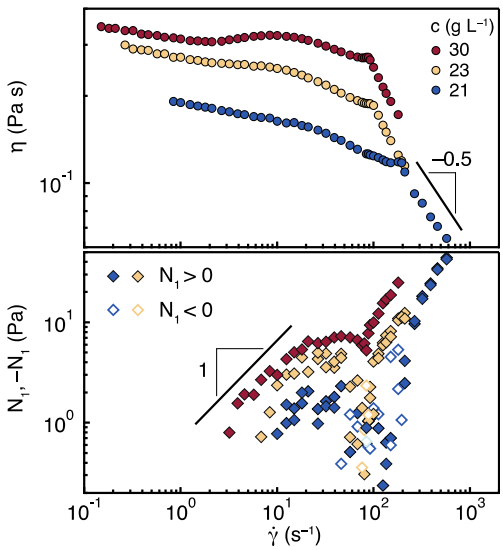

Fig. 3 Steady-state η (top) and N_1 (bottom) of fully nematic PBDT solutions in D_2O at solution concentrations of 21, 23, and 30 g L^{-1}. The data have been measured by starting from the highest shear rate shown, and decreasing in a stepwise fashion. Two curves are shown for the N_1 data for 21 and 23 g L^{-1}, measured on the same solution in a stepwise decreasing manner, to check for sample hysteresis and measurement uncertainty. Open diamond symbols (bottom) indicate negative N_1 values. Power laws are given in the figures as a guide to the eye

If we take the limiting value of the viscosity at low shear rates as an indication of the zero-shear viscosities, i.e., a region II plateau, solution concentrations for which fully nematic phase behavior is observed show a monotonic increase in viscosity with concentration. The Doi-Edwards theory predicts an increase in the local orientational order from the increasing strength of the nematic potential, thus reducing the viscosity of the nematic (Doi and Edwards 1986). The increasing viscosity with concentration suggests that the local orientational order does not increase significantly over this concentration regime. The increasing viscosity with concentration could arise from two effects, textural or viscous stresses, which are both monotonically increasing functions with concentration (Larson 1996). However, we will show later that the effect of textural elasticity in the shear rate regime we investigate here is not dominant, due to the lack of strain scaling of flow reversal experiments that we observe in the low shear rate regime. As such, we suggest that the increasing viscosity with concentration in this regime relates to the increasing contribution of viscous stresses to the total shear stress.

Instead of a monotonic and smoothly decreasing viscosity with shear rate, as observed for quiescently isotropic solutions, the viscosity of the 21 g L^{-1} solution develops a slight plateau at moderate shear rates of 3–30 s^{-1}, before shear thinning more rapidly up to another region that shows a hesitation in the viscosity. At 30 g L^{-1}, the viscosity even exhibits an increase over this shear rate regime, i.e., shear thickening behavior. In this regime, N_1 increases linearly with shear rate and reaches a local maximum that increases in magnitude with concentration, consistent with prior observations (Baek et al. 1993b; Kiss and Porter 1980).

At shear rates in the 80–200-s^{-1} range, we observe a pronounced kink, or hesitation, in the viscosity and the emergence of a negative N_1 regime for the 21 and 23 g L^{-1} solutions, or positive dip at 30 g L^{-1}. To better visualize this range,

we replot the steady-state viscosity flow curve data from Fig. 3 in Fig. 4 in a semi-log representation. For liquid crystalline PBDT solutions in D_2O, this hesitation regime is quite well-defined and pronounced, as compared to the broad hesitation in the flow curve observed in liquid crystalline PBG (Kiss and Porter 1978, 1980; Maffettone et al. 1994). The arrows in Fig. 4 indicate, for each concentration, the shear rate at the minimum N_1 value.

This hesitation in the viscosity is a classic signature of the flow behavior of nematic LCPs under shear that originates from a broadening of the molecular orientational distribution function (ODF) (Larson 1990; Marrucci and Maffettone 1989). At shear rates higher than the minimum N_1 value, the director is supposed to adopt a stationary angle with respect to the flow direction, rather than undergo periodic oscillations. It is noticeable here that we not only observe a pronounced hesitation, but a very narrow regime where the viscosity undergoes slight shear thickening, observed at 21 and 30 g L^{-1}, immediately prior to high shear rate shear thinning (flow alignment). This very narrow regime of shear thickening was confirmed by measuring a 2nd flow curve on the same solutions, and with separately loaded, independent solutions. Numerical simulations by Forest et al. (Forest et al. 2004a; Forest et al. 2004b) have predicted a very narrow regime of shear rates that correspond to a director state, called the out-of-plane steady (OS) regime, where the director adopts a stationary angle out of the shear plane and at a slightly negative angle with respect to the flow direction. This OS state is predicted to exhibit slight shear thickening immediately prior to shear thinning associated with flow alignment. Later, we will show that the shear rates that exhibit this shear thickening do not exhibit oscillating stress transients following step-down, consistent with a stationary director state. To the best of our knowledge, this result provides the first experimental evidence for the existence of the OS director state, although this assignment is consistent yet not definitive.

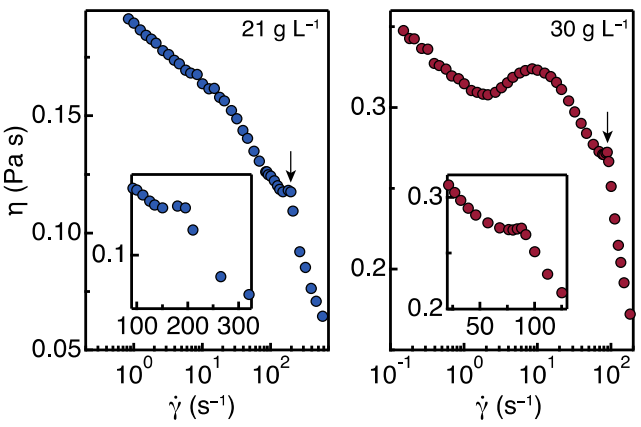

Fig. 4 Semi-log representation of the steady-state viscosity as a function of shear rate for nematic PBDT solutions in D_2O. The insets show the same data on linear axes in the vicinity of the transition to flow alignment, more clearly showing the slight shear thickening behavior in that regime

We previously reported nonlinear flow curves of the same PBDT solutions in water, and also found steady-state shear thickening at moderate shear rates (Fox et al. 2020a), similarly observed here. The magnitude of the shear thickening response is significantly smaller in D_2O than in water. The suppression of shear thickening in D_2O, compared to water, was confirmed by repeated measurements on solutions with nearly identical concentrations from the same polymer batch. Moreover, the sudden increase in viscosity, which we tentatively assigned as an OS director state, did not appear in the rheological measurements in water. However, we cannot exclude the existence of the slight shear thickening in water prior to flow alignment because the regime appears to occur over an extremely narrow shear rate regime.

To the best of our knowledge, this isotope effect on the rheology of a LCP has not been previously reported, although it may arise from several factors that are known to be different in D_2O as compared to water. The enhanced local structure of D_2O stiffens the solvation shell and may lead to an enhancement of the persistence length (López-Barrón and Wagner 2011). Alternatively, the differences between water and D_2O in solvent viscosity (Jones and Fornwalt 1936) may cause a subtle change in the polymer-solvent friction coefficient. We also observed degradation of the viscosity for PBDT solutions in D_2O if the sample experienced shear rates far above the onset of flow alignment. As such, we have limited the shear rates investigated to ranges over which the viscosity did not exhibit measurable hysteresis over the course of the rheological experiments. We speculate that rod breakage, resulting in a reduction in the average length of PBDT rods, occurs at high shear rates in D_2O leading to this viscosity reduction.

We note that the shear rate for the hesitation in the viscosity and subsequent onset of flow alignment in PBDT solutions exhibits an anomalous trend with concentration than predicted by theory. For PBG in m-cresol, increasing the solution concentration results in a monotonic shift of the N_1 regime to higher shear rates (Kiss and Porter 1978, 1980). The increase in concentration results in an increase in the strength of the nematic potential acting upon individual rod-like polymers, and enhances the local molecular orientation. This reduction in misalignment of the rods due to an increase in the nematic potential requires a larger shear flow to induce a reduction in the molecular ODF, thus increasing the shear rate for the onset of negative N_1 and the viscosity hesitation.

For HPC in *m*-cresol at solution concentrations up to 35 wt%, the shear rate for the minimum in N_1 increases with concentration (Baek et al. 1993b), similar to PBG (Kiss and Porter 1978, 1980). At solution concentrations between 35 and 50 wt%, the shear rate for the minimum in N_1 reverses trend, and decreases with increasing concentration. At 55 wt%, the negative N_1 regime is eliminated, but a positive local minimum remained, creating a dip in the shear rate dependence of N_1. Baek et al. (1993b) proposed that the

increasing influence of the viscous contribution to the stress tensor explains the elimination of the negative N_1 regime, while maintaining a positive dip in N_1. At a given dimensionless shear rate $\dot{\gamma}/D_r$, the ratio of the viscous to elastic stress contributions is controlled by the parameter $\beta_V = \zeta_{str} D_r / k_B T$. Initial considerations of the concentration dependence of β_V would indicate that it should be constant, as $D_r \sim \zeta_{str}^{-1}$ (Doi and Edwards 1986). However, at high enough solution concentrations, the increasing importance of polymer-polymer friction may lead to an increasing ζ_{str} without a corresponding decrease in D_r, causing β_V to increase with concentration. The calculations of these authors showed that an increasing β_V resulted in the elimination of a negative N_1 regime, while a positive dip in N_1 remains, as observed experimentally (Baek et al. 1994). However, this rationale does not explain the complete elimination of a local minimum in N_1, since the viscous stress contribution itself exhibits a local minimum in N_1. Thus, the effect of increasing polymer concentration may not only change β_V, which modulates the reduction in N_1 at shear rates that broaden the molecular ODF, but also the director state may in fact change. Indeed, numerical simulations of the director phase space shows that, near the fully nematic phase boundary, slight changes in concentration dramatically influence the selected director state (Forest et al. 2004a; Forest et al. 2004b).

We plot the steady-state viscosity and N_1 for 38 and 45 g L^{-1} solutions in Fig. 5. Power law fits to the low shear rate data in comparison to the prediction for region I shear thinning (− 0.5) suggest that the observed behavior does not originate from elasticity associated with the polydomain defect texture. The most noticeable feature is the presence of the clearly observable shear thickening regime at moderate shear rates, further confirming our observations at lower concentrations. Moreover, we find that the hesitation in the viscosity that we observed at lower concentrations prior to shear thinning at high shear rates is absent. Rather than a regime of negative N_1, we observe a positive dip in N_1 at 38 g L^{-1} over the shear rate range of 50–100 s^{-1}, before increasing again at higher shear rates. At 45 g L^{-1}, this dip in N_1 is eliminated and we observe a monotonically increasing N_1, which scales nearly linearly over two decades in shear rate. That is, the rheological signatures associated with director wagging, which manifests as a negative N_1 signal, become suppressed and subsequently eliminated as the solution concentration is increased to 38 and 45 g L^{-1}, respectively.

Segmental alignment from Rheo-SANS

We investigated the shear-induced alignment of PBDT in D_2O using rheology and in situ small-angle neutron scattering (rheo-SANS) at the Extended Q-Range SANS (EQSANS) instrument at Oak Ridge National Laboratory. Liquid

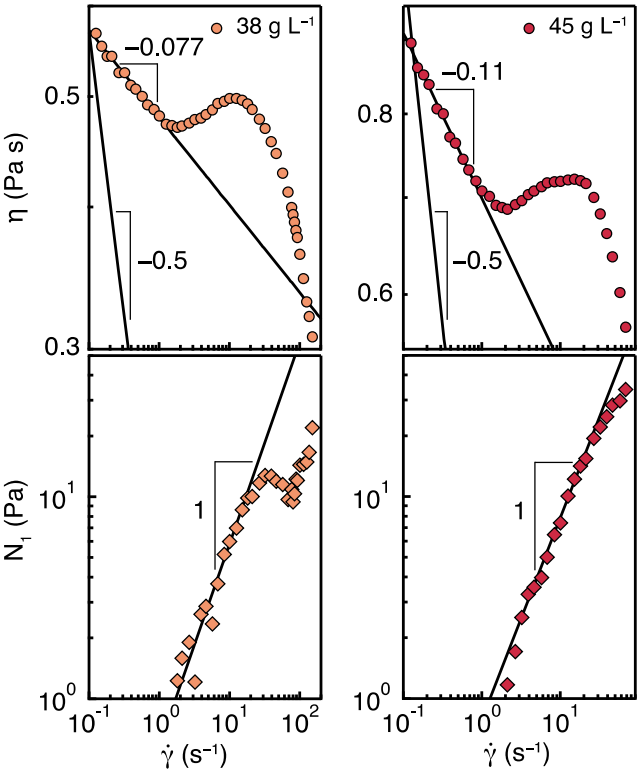

Fig. 5 Steady-state viscosity and N_1 of liquid crystalline PBDT in D_2O as a function of shear rate for 38 and 45 g L^{-1}. All axes are on a logarithmic scale. Power law fits to the viscosity at low shear rate show weak shear thinning exponents (approximately − 0.1), and are compared to the prediction for region I shear thinning of − 0.5. Linear fits to the N_1 data are shown, evidencing the positive dip in N_1 for the 38 g L^{-1} solution, and a monotonically increasing N_1 for the 45 g L^{-1} solution

crystalline solutions were sheared using a Couette geometry, where the incident neutron beam was parallel to the velocity gradient direction, yielding the scattering patterns to be a projection in the 1–3 plane (flow–vorticity plane). The 2D scattering patterns of a representative 30 g L^{-1} solution are given in Fig. 6(a) at shear rates of 1, 10, and 100 s^{-1}, and each 2D scattering pattern has identical intensity scaling. Consistent with previous scattering data on PBDT solutions, we observe a scattering peak from the structure factor that corresponds to the intermolecular rod-rod distance (Wang et al. 2014, 2019). Under low shear rates, we observe substantial scattering anisotropy that is localized along the vorticity axis, indicating that the time-averaged director orientation is aligned along the flow direction. Increasing the shear rate causes the scattering anisotropy to increase in sharpness along the vorticity axis, indicating an increase in the time-averaged degree of orientation along the flow direction.

We quantified the orientational order by performing azimuthal intensity integrations within a narrow q-range that contained the structure factor peak, corresponding to the lateral rod-rod correlation length, shown by the dashed red lines in Fig. 6(a). We fit the azimuthal intensity dependence within this q-range with a Maier-Saupe type distribution function to

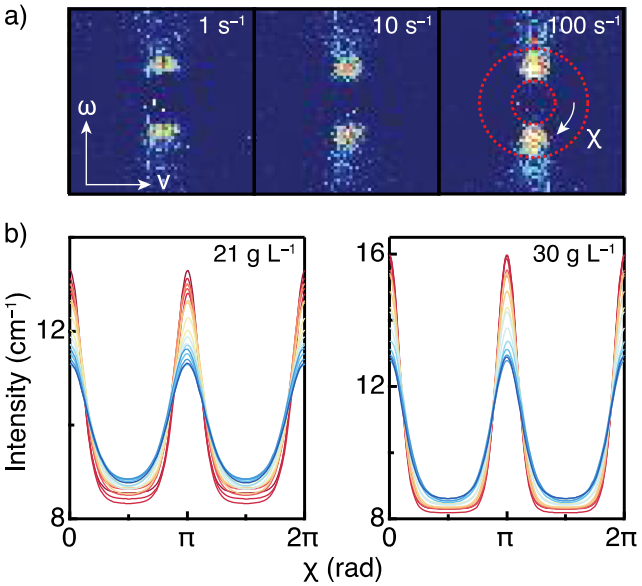

Fig. 6 **a** 2D rheo-SANS patterns of PBDT in D_2O at 30 g L^{-1} under shear rates of 1, 10, and 100 s^{-1} projected in the 1–3 shear plane. The flow (v) and vorticity (ω) directions are shown by the arrows. **b** Maier-Saupe fits to the azimuthal intensity dependence over the q-range corresponding to the intermolecular structure factor peak at 21 and 30 g L^{-1}. Blue to red colors indicate increasing shear rates from 1–460 s^{-1} to 0.21–210 s^{-1} for 21 and 30 g L^{-1}, respectively

calculate apparent order parameter in the 1–3 plane, S_{13}, described previously (Picken et al. 1990) and commonly employed to quantify the degree of orientation under shear (Viale et al. 2004b). As such, the parameter S_{13} reports on the anisotropy of intermolecular center-to-center mass correlations, not the intramolecular ODF. For the purposes of this work, this method of analysis is sufficient to draw the necessary conclusions from our rheo-SANS measurements regarding changes in bulk alignment under shear. We stress that this procedure does not provide a rigorous description of the 3D ODF, which can be obtained through model-independent methods (Huang et al. 2019).

Here, we simply utilize this method to obtain a qualitative description of the time- and spatially averaged rod orientation in the 1–3 projection under shear. Note that S is proportional to the product of the molecular order parameter, S_m, and the order parameter of the mesoscopic nematic domains, $\overline{S}$ (Picken et al. 1990). In Fig. 6(b), we show the resulting Maier-Saupe fits to the integrated azimuthal intensity for 21 and 30 g L^{-1}, where the shear rate increases from blue to red. The underlying data and fits are shown for each shear rate in Figure S5 and Figure S6. Note that the azimuthal integration (χ= 0 rad) begins along the vorticity axis, such that intensity maxima are observed at angles of 0 and π radians. As can be observed, the degree of anisotropy increases with the applied shear rate, corresponding to increased orientation. The shear rate dependence of S_{13} obtained from the Maier-Saupe fits to the azimuthal scattering anisotropy is plotted along with the steady-state viscosity in Fig. 7 for solution concentrations of 21, 30, and 45 g L^{-1}. The absolute values of S_{13} are high compared to rheo-SANS data obtained on liquid crystalline solutions of PBG (Walker and Wagner 1996) or HPC (Keates et al. 1993). Interestingly, S_{13} is significantly higher than nematic solutions of sulfo-PPTA under shear, which plateaus near 0.55 at shear rates in excess of 1000 s^{-1} (Viale et al. 2004b).

At 21 g L^{-1}, S_{13} appears to approach a plateau value at low shear rates, although the scatter in the data makes this conclusion tentative, while the viscosity exhibits weak shear thinning. At a shear rate of 10 s^{-1}, S_{13} begins to steadily rise from ~0.45 to ~0.65 as the viscosity exhibits a break and shear thins more strongly with increasing shear rate. The slight increase in viscosity at a shear rate of 195 s^{-1} appears to correlate with a local reduction in S_{13}, before again increasing up to greater than 0.8 at the highest shear rates investigated. Presumably, higher shear rates would result in a plateau in the measured S_{13}, but we limited our shear rates investigated in rheo-SANS due to the viscous heating at high shear rates that can only be controlled by air cooling.

At 30 g L^{-1}, S_{13} appears to decrease at low shear rates, but we caution against deeper interpretation of the trends observed at low shear rates because of the noise in the data. Above a shear rate of 1 s^{-1}, S_{13} exhibits a steady increase from ~0.6 to ~0.85 at 46 s^{-1}, while the viscosity exhibits moderate shear thickening, followed by shear thinning behavior. At slightly higher shear rates where we observe the slight and sudden

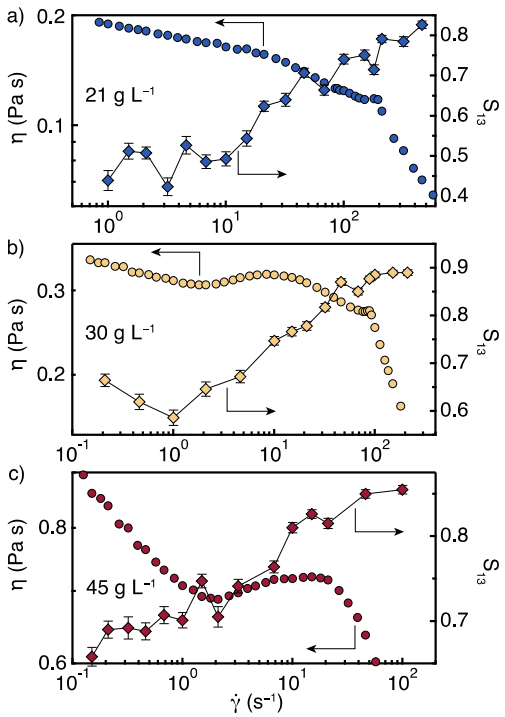

Fig. 7 Steady-state viscosity (left axis, circles) and 1–3 plane apparent order parameter (right axis, diamonds) as a function of shear rate for (a) 21, (b) 30, and (c) 45 g L^{-1}. Note that the viscosity axis is on a logarithmic scale

increase in viscosity just prior to shear thinning, S_{13} undergoes a similarly sudden reduction, before increasing to reach a saturation value of ~ 0.9 at higher shear rates.

At 45 g L^{-1}, S_{13} exhibits a near monotonic increase from shear rates of 0.1 up to 100 s^{-1}. Two local minima in S_{13} correspond to the beginning and peak of shear thickening behavior in the steady-state viscosity, although the data point density from this data prohibits us from certainty in these features. From this data, however, we do conclude that the shear thickening in the steady-state flow curves is correlated with an increase in S_{13}. In addition, we do not observe any signature of director logrolling (a director state that also causes shear thickening), which would manifest as a rotation of the scattering anisotropy from along the vorticity (vertical in Fig. 6(a)) to along the flow direction (horizontal in Fig. 6(a)), i.e., a change in average rod orientation from along the flow direction to along the vorticity axis. The hesitation in the viscosity, and sudden increase immediately prior to flow alignment, appears well correlated with a local reduction in S_{13}.

The fact that the shear thickening regime occurs along with an increase in S_{13} is counter-intuitive, as one expects increasing orientational order to correlate with decreasing viscosity. However, in LCPs, both the microscopic and mesoscopic orientational distribution functions must be taken into consideration (Burghardt 1998). For example, a decrease in the local order parameter occurs at the tumbling-to-wagging transition, but can simultaneously occur with an increase in the mesoscopic domain order parameter. If the mesoscopic domain order parameter increase is greater than the decrease in the local order parameter, this cumulative effect would then act to increase S_{13}.

Here, we suggest the following picture to explain the observed S_{13} trend and connect it to the steady-state viscosity flow curve. We have proposed that the origin of shear thickening occurs due to director kayaking (Fox et al. 2020a), as predicted by prior numerical simulations (Forest et al. 2004a; Forest et al. 2004b). The scattering spectra of director kayaking in the 1–3 plane would appear as if the director is, on average, aligned along the flow direction with some angular distribution, as observed here. Increasing the shear rate may influence the rotational frequency of the kayaking orbit, such that the rods spend more time with their axis pointed close to the flow direction. This longer time for rotation of the kayaking orbit would increase S_{13} as measured by rheo-SANS. At high shear rates prior to flow alignment, in the hesitation regime of the flow curve and at the point where the viscosity undergoes a slight, second shear thickening, we consistently observe that S_{13} undergoes a local minimum. In the next section, we show that this shear rate corresponds to a non-oscillatory response of the shear stress upon flow reversal. As such, we suggest that this measured reduction in S_{13} is correlated with a stationary out-of-plane director state, also predicted by the numerical simulations of Forest et al. (Forest et al. 2004b) to exist just below the shear rate for the onset of flow alignment.

Transient rheology of the nematic phase

Transient rheological experiments are useful in interpreting the behavior of the nematic director that invariably dictate the steady-state rheological response. Thus, we investigated the 21 g L^{-1} solution using flow reversals, where the direction of the shear is suddenly reversed at constant shear rate. In this transient experiment, it is thought that the sudden change in flow direction causes a 180° flip of the director, inducing coherence of the oscillating nematic directors that then gradually dephase due to interdomain interactions (Larson and Doi 1991). In Fig. 8(a), we plot the transient shear stress, normalized to the steady-state value, as a function of applied strain following flow reversal. To aid visualization, we have separated the data into separate subplots and indicate the shear rate used (and corresponding color of stress transient) in the figure.

We do not observe strain-scaling behavior in the flow reversal experiments over any shear rate range, further suggesting that these solutions are not strongly affected by the nematic texture. At low shear rates (0.84–13 s^{-1}), the data can be described as a damped oscillatory pattern, exhibiting 2 to 3 peaks before reaching the equilibrium stress value at strains greater than approximately 100. This qualitative description of the transient stress following flow reversal is the same as that observed for liquid crystalline solutions of PBG (Moldenaers et al. 1989) in the linear regime of the flow curve. However, as the shear rate is increased through this regime, the normalized stress values of the first two peaks decreases and shifts to larger strain values, resulting in non-strain-scaling behavior.

In the moderate shear rate regime (13–46 s^{-1}), the normalized stress of the first peak continues to decrease, but eventually reaches a plateau values, while the second peak increases throughout this shear rate regime. As the shear rate is increased past 57 s^{-1}, the normalized stress value of the first peak, which reached a plateau value in the prior range, begins to increase while the second peak decreases in value. Both peaks begin to shift to larger strain values and a rapid increase in the oscillation period occurs over this range. At a shear rate of 125 s^{-1}, we observe the emergence of strongly oscillating stress transient that is suppressed when the shear rate is slightly increased to 150 s^{-1}. That is, strong oscillatory stress transients are only observed over a very narrow range of shear rates, close to, but below, the minimum in the steady-state N_1 and the sudden increase in viscosity for this concentration (see Fig. 3 and Fig. 4).

To provide some quantitative description of the evolution of the stress transients observed in the flow reversal experiments, we plot the normalized stress value of the first and second stress peak in Fig. 8(b) (*top*). In addition, the oscillation period of the stress transients, as measured by twice the

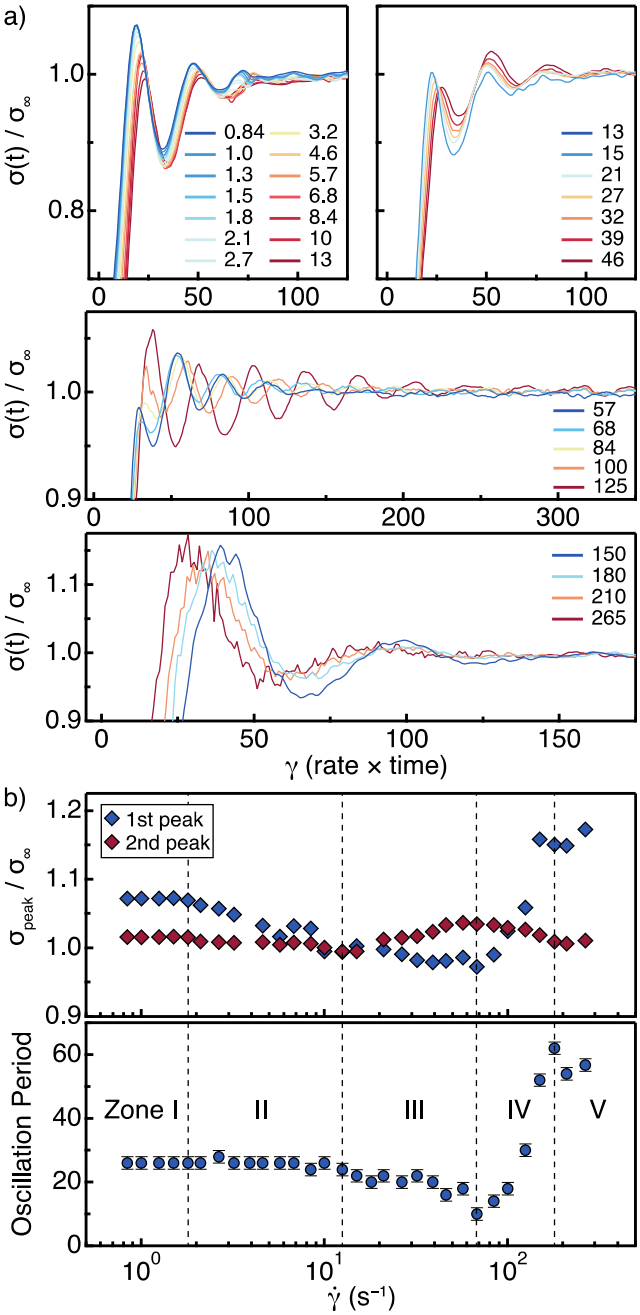

Fig. 8 **a** Transient shear stress following flow reversal for 21 g L^{-1} solution. The shear rates are given in the figure legend. **b** Normalized stress value of first peak (*top*) and oscillation period in strain units (*bottom*) as measured by twice the distance between the first peak and first valley. Error bars for the oscillation periods are estimated as ± 1 strain unit

strain period between the first peak and first valley, we similarly plot in Fig. 8(b) (*bottom*). Comparison of these two data sets with the qualitative evolution of the stress transients leads us to divide the data into five distinct zones, labeled and delineated by the dashed vertical lines.

As the shear rate is reduced towards zone I and lower, the normalized stress peaks and oscillation periods approach plateau values. However, as observed in the transient data, they are not strain-scaling because the entire transient curve shifts to larger strains with increasing shear rate. As such, it is unclear if strain-scaling behavior will be recovered at lower shear rates, but the low torque values and large strains required for reaching a steady state limit our experimental investigation.

In zones II and III, the oscillation period decreases, first slowly, then more rapidly, and reaches a minimum at 68 s^{-1}. Moreover, the changes in the relative magnitude of the first and second stress peaks upon flow reversal between zones II and III suggest that a qualitative change in the nature of the tumbling dynamics occurs over this shear rate regime.

The strongly oscillating stress transient behavior of zone IV appears to be similar to results attributed to the so-called wagging regime, identified previously in PBG (Grosso et al. 2003, Mewis et al. 1997) and *fd* virus suspensions (Lettinga and Dhont 2004; Lettinga et al. 2005). In this zone, both the normalized stress overshoot and the oscillation period, i.e., strain period of the director oscillations, both increase dramatically over a narrow shear rate regime. As the shear rate is increased past the wagging regime into zone V, we conclude the director achieves stationary flow alignment as evidenced by the non-oscillating stress transients and transition from decreasing to increasing steady-state N_1 values.

To further probe the evolution of the nematic director of nematic PBDT under flow across the flow curve, we utilized transient step-down experiments. In a step-down experiment, the solution is sheared until a steady state is reached in the flow alignment regime, where the director adopts a stationary angle. After a steady-state stress is attained, the shear rate is suddenly reduced without changing direction. By monitoring the transient stress as a function of applied strain following the step-down, the data reports on the temporal evolution of the nematic director (Mewis et al. 1997). The transient behavior of LCPs in flow reversal and step-down experiments is intimately related. However, the effects are magnified in a step-down experiment as the difference in the dynamical behavior of the director of the initial and final states can be dramatically different, while in flow reversals they are identical (Mewis et al. 1997). We plot the results of this experiment for 21 g L^{-1} in Fig. 9(a–d), separating the stress transients into different plots for visual clarity.

The qualitative behavior of the transient stress following step-downs is similar to that observed in flow reversal experiments, but the effect of varying the final shear rate is more dramatic. It becomes clear from the evolution of the transient stress in Fig. 9(a), where the final shear rate is varied through zones I and II as identified in the flow reversal experiments (see Fig. 8(b)), that a particular dynamical response is increasing in magnitude while another is being suppressed as the shear rate is increased, shown by the two vertical arrows showing the direction of increasing shear rate. As the shear

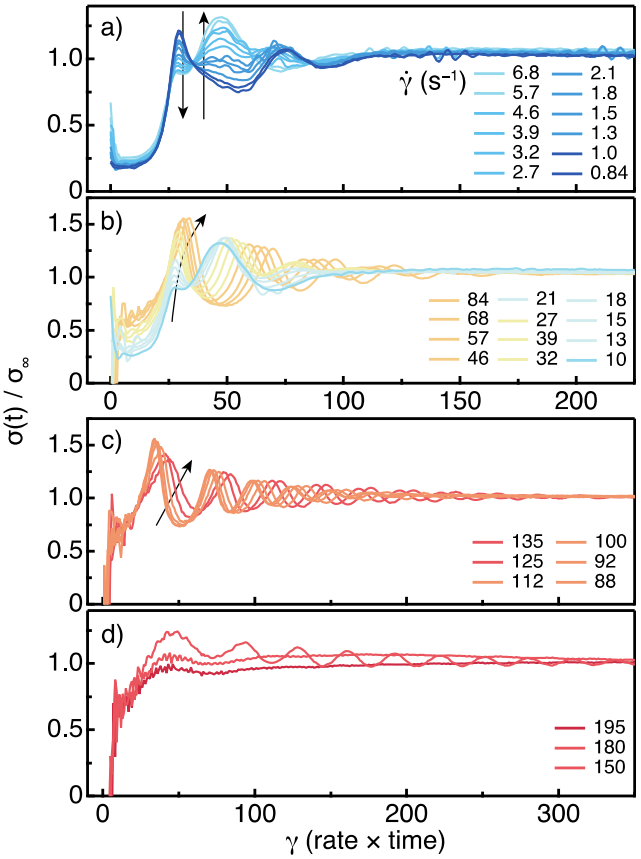

Fig. 9 Normalized stress transient following shear step-down from 570 s^{-1} to the shear rate indicated in the figure for 21 g L^{-1}. The arrows indicate increasing the value of the final shear rate following the step-down

rate is varied, a point along the strain axis maintains its normalized stress value, creating an effect similar to an isosbestic point, indicating that the system is changing linearly from one state to another (Greger et al. 2013). That is, the emergence of one director response upon shear step-down likely occurs at the expense of the prior state with a linear relationship in terms of their contribution to the shear stress. To the best of our knowledge, no experimental data of this nature on nematic LCPs, other than PBDT, has been reported in the literature (Fox et al. 2020a).

As the shear rate increases in Fig. 9(b), the stress overshoot of the first peak increases and the oscillations become less damped. This trend continues into Fig. 9(c), producing strong and persistent oscillating stress transients, most pronounced at a final shear rate of 135 s^{-1}. Figure 9(d) shows that the oscillations become increasingly suppressed as the final shear rate is increased above 150 s^{-1}. Note that the local maximum in the steady-state viscosity for 21 g L^{-1}, and minimum in N_1, occurs at a shear rate of 195 s^{-1} (see Fig. 3). At this final shear rate, we do not observe any oscillatory stress response following shear step-down. This is consistent with the results of Mewis et al., who found that the anomalous stress oscillations observed after shear step-downs were eliminated at the shear rate corresponding to the minimum in the steady-state N_1 (Mewis et al. 1997). Here, we suggest that the observed local maximum in the viscosity and minimum in N_1, as well as the elimination of oscillating stress transients, are due to the presence of an out-of-plane steady director state, as previously predicted in numerical simulations (Forest et al. 2004a; Forest et al. 2004b).

Increasing the solution concentration of PBDT causes the emergence of a broad shear thickening regime at moderate shear rates in the steady-state flow curve (see Fig. 3 and Fig. 4). To understand this behavior, we investigated the 30 g L^{-1} solution using the same shear step-down experimental protocol as performed for 21 g L^{-1}. We plot the transient stresses following step-downs for 30 g L^{-1} in Fig. 10, and separate the data into subplots for visual clarity. At 30 g L^{-1}, we observe shear thickening behavior in the steady-state viscosity over the shear rate regime of 2.1–21 s^{-1}, while N_1 is still an increasing function of shear rate, with the first local maximum of N_1 occurring at a shear rate of 46 s^{-1} (see Fig. 3). Comparison of the transient data from the two concentrations indicate that the evolution in the stress transients at low shear rates is qualitatively similar. The initial transient consists of a peak, valley, and second peak before being damped to its equilibrium stress value. As the shear rate increases, the behavior transitions smoothly into a transient that exhibits an initial shoulder followed by a broad maximum and minimum, before reaching the equilibrium stress value. The point of constant normalized stress upon increasing shear rates from 0.84 to 3.2 s^{-1} is also observed at 30 g L^{-1}, as seen in the lower concentration.

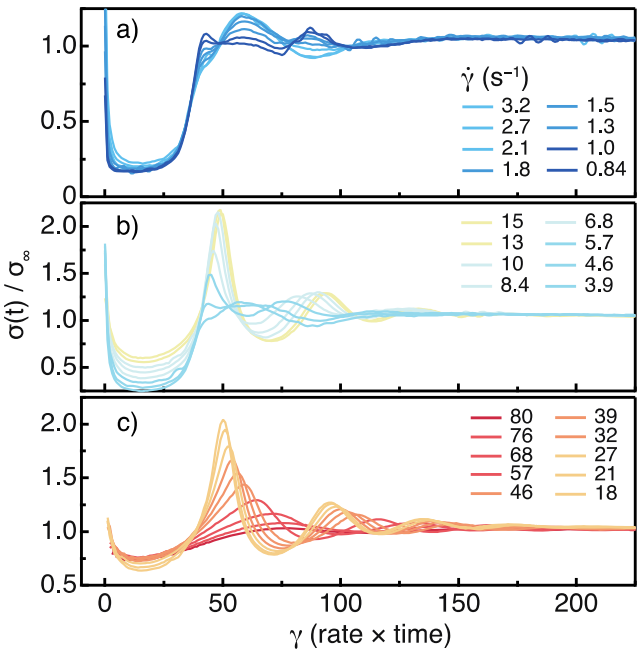

Fig. 10 Normalized stress transients following step-down from an initial shear rate of 180 s^{-1} for 30 g L^{-1}. The peak in the steady-state viscosity occurs at ~ 15 s^{-1}, and the dip in the steady-state N_1 occurs over the shear rate range of 46–88 s^{-1}

The most striking difference between the two concentrations is that the magnitude of the stress overshoot of the first peak for 30 g L^{-1}, which are significantly higher than observed at 21 g L^{-1}, reaching over two times the equilibrium stress value. The maximum value of the stress overshoot occurs at a shear rate that is close to the peak in the shear thickening of the steady-state viscosity. The qualitative behavior of the transient stress following step-down, with extremely large stress overshoots, is not consistent with the observed behavior that has been assigned as director wagging in other systems (Grosso et al. 2003; Lettinga et al. 2005; Mewis et al. 1997). Moreover, note that the positive dip in N_1 for 30 g L^{-1}, which has been correlated with the existence of director wagging (Baek et al. 1994), spans the shear rate regime of 46–88 s^{-1}, clearly occurring at higher shear rates than the large stress overshoots.

We extract further information about the nature of the director responses by investigating how the transient N_1 signal evolves after the shear step-down, and its relation to the shear stress. We plot the transient shear stress (as in Fig. 9) and N_1, after subtraction of the steady-state N_1 value, for a select group of shear rates in Fig. 11. For completeness, we give the transient shear stress and N_1 data for every shear rate investigated for 21 g L^{-1} in Figure S7 and Figure S8, and for 30 g L^{-1} in Figure S9 in the Supporting Information.

At final shear rates of 27 and 68 s^{-1}, we observe the onset of strong negative deviations in the transient N_1 signal following step-down and the emergence of a damped oscillatory pattern similar to the behavior in the shear stress. In general, the peaks in the shear stress follow the minimum in N_1, in terms of their strain position, following shear step-down. Moreover, the strain periods of oscillations of the shear stress and N_1, as measured by the peak-to-peak distance, are identical within experimental uncertainty. However, as the final shear rate is increased to 135 s^{-1}, the oscillations in the transient shear stress and N_1 data broaden and become more sustained, extending out to over 300 strain units before damping down to the final steady state.

The microscopic origin of the viscoelastic behavior of LCPs can arise from either elastic or viscous contributions to the stress tensor. Elastic stresses arise from distortions of the molecular ODF, while viscous stresses originate from polymer-solvent frictional forces, as discussed previously. To understand the relative magnitudes of these two stress contributions, Maffettone et al. performed numerical simulations in the high shear rate regime in transient flow reversal, and step-up and step-down experiments (Maffettone et al. 1994). Their simulations showed that construction of so-called dynamic stress paths, i.e., transient N_1 versus shear stress, indicates the relative importance of the elastic and viscous stresses by the "chirality" of the stress path. In this representation, the chirality refers to the direction of the stress path rotation, either clockwise or counterclockwise. In the case of purely elastic

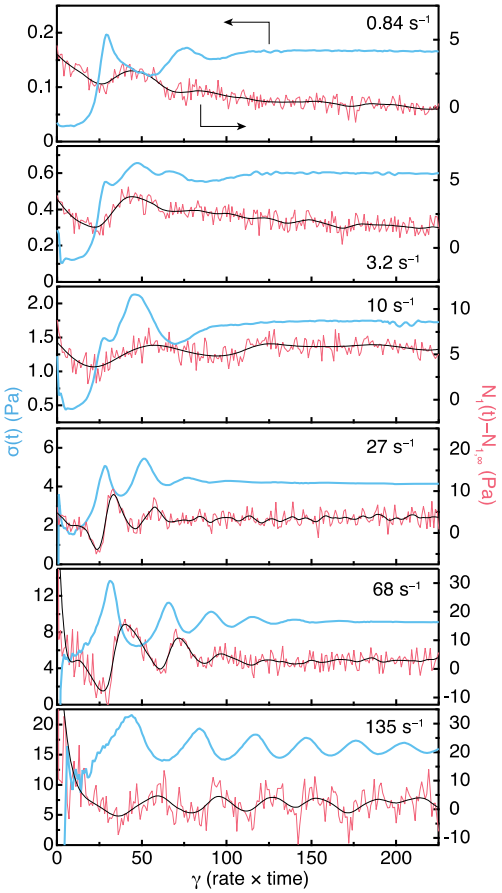

Fig. 11 Shear stress (blue, left) and N_1 after subtraction of the steady-state N_1 value (red, right) transients following shear step-down from 570 s^{-1} to the final shear rate indicated in the figure legend. The sample concentration is 21 g L^{-1}. The black lines are smoothed fits to the raw N_1 for visual clarity

stresses, the stress paths exhibited clockwise rotations, while conversely for purely viscous stresses. If a combination of elastic and viscous stress contributions is present, the direction of rotation of the stress path may undergo an inversion during the transient experiment. The authors compared their numerical simulations to experiments on liquid crystalline PBG in *m*-cresol. In all transient flow experimental protocols, including flow reversals and shear step-downs, the stress paths exhibited a counterclockwise rotation. This led to the conclusion that the viscous stress contribution is dominant at high shear rates. Moreover, the parameter β_V, which is a measure of the relative importance of the viscous to elastic stresses, was thus estimated to be near the dilute limit, i.e., $\beta_V = 0.15$ for PBG in *m*-cresol. Later work by Larson reassessed the relative magnitudes of the viscous and elastic stresses by analyzing the concentration dependence of the viscosity over the I-N transition and in the fully nematic phase and estimated $\beta_V = 0.03$, which is about five times smaller than the dilute limit (Larson 1996). Moreover, Larson found that the chirality of the stress path for determining the dominance of elastic or viscous stresses is only valid in region III, and not in the region II

plateau. For PBDT, we have already concluded that the investigated shear rate regime is within region III.

Thus, to elucidate the nature of the observed shear thickening behavior, we constructed dynamic stress paths from the shear step-down experiments for c = 21 and 30 g L^{-1} in Fig. 12(a) and (b), respectively. The arrow heads along the stress paths indicate the direction of increasing strain following the step-down. For all stress paths, we plot the first 200 strain units to capture the initial transient stress information, which is sensitive to the nematic director's response as it evolves from a flow-aligned state to a stable director state at lower shear rates. The shear rates for the 21 g L^{-1} solution all correspond to shear thinning regimes in the steady-state flow curve. For the 30 g L^{-1} solution, which exhibits pronounced shear thickening, the three shear rates correspond to immediately prior to, at the peak, and following the shear thickening regime in the steady-state flow curve.

From inspection of these dynamic stress paths, we conclude that the dominant behavior is for the stress paths to undergo counterclockwise rotation for both concentrations. At the lower shear rate shown for each concentration, this counterclockwise rotation is delayed, and the stress path appears to undergo at least part of a clockwise rotation before settling into its counterclockwise pattern. As noted by Maffettone et al., the relative importance of the elastic and viscous stresses may change along the stress transient and both contribute to the transient (Maffettone et al. 1994); as such, we interpret this observation to indicate that the elastic stress contribution is more important at the lower shear rates. Importantly, our data shows that at the peak of the shear thickening regime (10 s^{-1} for c = 30 g L^{-1}), the dynamic stress path is a clear counterclockwise rotation. Using the framework set forth by Maffettone et al. to interpret these data (Maffettone et al. 1994), we conclude that the origin of the steady-state shear thickening lies with the viscous stress contribution arising from the motions associated with the kayaking director state (Forest et al. 2004a; Forest et al. 2004b). The behavior of the stress paths is inconsistent with shear thickening from an elastic effect, i.e., a broadening of the molecular ODF due to the wagging state, that has been suggested to be the origin of shear thickening observed in nematic *fd* suspensions (Lettinga and Dhont 2004; Lettinga et al. 2005).

In conclusion, we have presented transient and steady-state rheological data of charged, rod-like sulfo-aramid assemblies

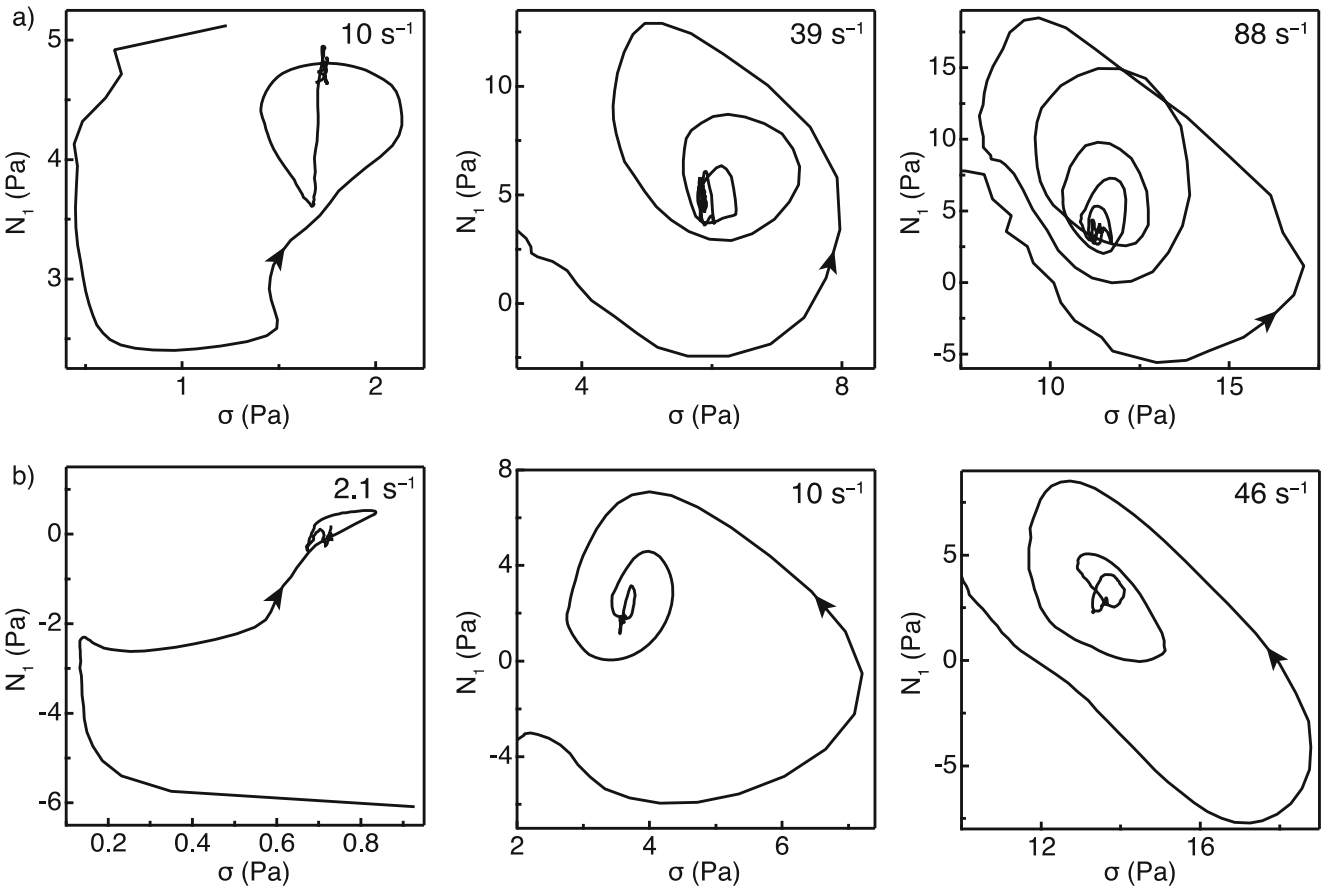

Fig. 12 Transient stress paths following shear step-down for **a** 21 g L^{-1} from an initial shear rate of 570 s^{-1}, and **b** 30 g L^{-1} from an initial shear rate of 180 s^{-1}. The first 200 strain units are plotted, and the direction of increasing strain is indicated by the arrow heads. The final shear rates are indicated in the figures

in the isotropic and nematic phases. The concentration scaling behavior of the viscosity, relaxation time, and terminal modulus of the isotropic solutions shows distinct regimes of power law behavior, with deviations from the predictions of Doi-Edwards theory for hard rods. The flow curves of nematic PBDT solutions exhibit an unusual shape, with two regimes of distinct shear thickening behavior. Using rheo-SANS and transient rheological measurements, we suggest the origins of these shear thickening regimes as director kayaking and out-of-plane steady states, respectively. We analyzed the transient rheological shear step-downs by constructing dynamic stress paths, which indicate a dominance of the viscous stress contribution to the observed shear thickening that arises from director kayaking. These results provide new insight into the nonlinear rheological behavior of nematic liquid crystalline polymers under shear.

Acknowledgments R. J. F., M. G. F., and T. J. D. acknowledge support from The University of North Carolina at Chapel Hill Creativity Hubs award. M. G. F. acknowledges support from the National Science Foundation under award number DMS-1517274. This material is based upon work supported by the U.S. Department of Energy, Office of Science, Office of Workforce Development for Teachers and Scientists, Office of Science Graduate Student Research (SCGSR) program. The SCGSR program is administered by the Oak Ridge Institute for Science and Education (ORISE) for the DOE. ORISE is managed by ORAU under contract number DE-SC0014664. A portion of this research used resources at the Spallation Neutron Source, a DOE Office of Science User Facility operated by the Oak Ridge National Laboratory. This material is based upon work supported by, or in part by, the U.S. Army Research Laboratory and the U.S. Army Research Office under contract number W911NF-16-1-035. This work was performed in part at the Duke University Shared Materials Instrumentation Facility (SMIF), member of the North Carolina Research Triangle Nanotechnology Network (RTNN), which is supported by the National Science Foundation, Grant ECCS-1542015, as part of the National Nanotechnology Coordinated Infrastructure (NNCI).

Data availability All data generated or analyzed during this study are included in this published article and its supplementary information files.

Compliance with ethical standards

Disclaimer All opinions expressed in this paper are the authors' and do not necessarily reflect the policies and views of DOE, ORAU, or ORISE.

Conflict of interest The authors declare that they have no conflict of interest.

References

Baek SG, Magda JJ, Cementwala S (1993a) Normal stress differences in liquid crystalline hydroxypropylcellulose solutions. J Rheol 37: 935–945. https://doi.org/10.1122/1.550404

Baek SG, Magda JJ, Larson RG (1993b) Rheological differences among liquid-crystalline polymers I The first and second normal stress differences of PBG solutions. J Rheol 37:1201–1224. https://doi.org/10.1122/1.550377

Baek SG, Magda JJ, Larson RG, Hudson SD (1994) Rheological differences among liquid-crystalline polymers. II. Disappearance of negative N1 in densely packed lyotropes and thermotropes. J Rheol 38: 1473–1503. https://doi.org/10.1122/1.550555

Baird DG, Ballman RL (1979) Comparison of the rheological properties of concentrated solutions of a rodlike and a flexible chain polyamide. J Rheol 23:505–524. https://doi.org/10.1122/1.549530

Bostwick JE, Zanelotti CJ, Iacob C, Korovich AG, Madsen LA, Colby RH (2020) Ion transport and mechanical properties of non-crystallizable molecular ionic composite electrolytes. Macromolecules 53:1405–1414. https://doi.org/10.1021/acs.macromol.9b02125

Burghardt WR (1998) Molecular orientation and rheology in sheared lyotropic liquid crystalline polymers. Macromol Chem Phys 199: 471–488

Dobrynin AV, Colby RH, Rubinstein M (1995) Scaling theory of polyelectrolyte solutions. Macromolecules 28:1859–1871

Doi M, Edwards SF (1978a) Dynamics of rod-like macromolecules in concentrated solution. Part 1. J Chem Soc Faraday Trans 2(74):560–570

Doi M (1981) Molecular dynamics and rheological properties of concentrated solutions of rodlike polymers in isotropic and liquid crystalline phases. J Polymer Sci Phys 19:229–243

Doi M, Edwards SF (1978b) Dynamics of rod-like macromolecules in concentrated solution. Part 2. J Chem Soc Faraday Trans 2(74):918–932

Doi M, Edwards SF (1986) The theory of polymer dynamics. Oxford University Press

Dou S, Colby RH (2006) Charge density effects in salt-free polyelectrolyte solution rheology. J Polym Sci B Polym Phys 44:2001–2013. https://doi.org/10.1002/polb.20853

Dou S, Colby RH (2008) Solution rheology of a strongly charged polyelectrolyte in good solvent. Macromolecules 41:6505–6510

Every HA, Janssen GJM, Sitters EF, Mendes E, Picken SJ (2006a) Performance analysis of sulfonated PPTA polymers as potential fuel cell membranes. J Power Sources 162:380–387. https://doi.org/10.1016/j.jpowsour.2006.07.002

Every HA, Mendes E, Picken SJ (2006b) Ordered structures in proton conducting membranes from supramolecular liquid crystal polymers. J Phys Chem B 110:23729–23735

Forest MG, Wang Q, Zhou R (2004a) The flow-phase diagram of Doi-Hess theory for sheared nematic polymers II: finite shear rates. Rheol Acta 44:80–93. https://doi.org/10.1007/s00397-004-0380-9

Forest MG, Wang Q, Zhou R (2004b) The weak shear kinetic phase diagram for nematic polymers. Rheol Acta 43:17–37. https://doi.org/10.1007/s00397-003-0317-8

Fox RJ, Yu D, Hegde M, Kumbhar AS, Madsen LA, Dingemans TJ (2019) Nanofibrillar ionic polymer composites enable high-modulus ion-conducting membranes. ACS Appl Mater Interfaces 11:40564–40574. https://doi.org/10.1021/acsami.9b10921

Fox RJ, Forest MG, Picken SJ, Dingemans TJ (2020a) Observation of transition cascades in sheared liquid crystalline polymers. Soft Matter 16:3891–3901

Fox RJ, Hegde M, Zanelotti CJ, Kumbhar AS, Samulski ET, Madsen LA, Picken SJ, Dingemans TJ (2020b) Irreversible shear-activated gelation of a liquid crystalline polyelectrolyte. ACS Macro Letters In Press

Funaki T, Kaneko T, Yamaoka K, Ohsedo Y, Gong JP, Osada Y, Shibasaki Y, Ueda M (2004) Shear-induced mesophase organization of polyanionic rigid rods in aqueous solution. Langmuir 20: 6518–6520

Gao J, Wang Y, Norder B, Garcia SJ, Picken SJ, Madsen LA, Dingemans TJ (2015) Water and sodium transport and liquid crystalline alignment in a sulfonated aramid membrane. J Membr Sci 489:194–203. https://doi.org/10.1016/j.memsci.2015.03.090

Gennes PGD, Prost J (1978) The physics of liquid crystals. Oxford University Press

Greger M., Kollar M., Vollhardt D. (2013) Isosbestic points: how a narrow crossing region of curves determines their leading parameter dependence. Phys Rev B 87. https://doi.org/10.1103/PhysRevB.87.195140

Grizzuti N, Cavella S, Cicarelli P (1990) Transient and steady-state rheology of a liquid crystalline hydroxypropylcellulose solution. J Rheol 34:1293–1310. https://doi.org/10.1122/1.550139

Grosso M, Crescitelli S, Somma E, Vermant J, Moldenaers P, Maffettone PL (2003) Prediction and observation of sustained oscillations in a sheared liquid crystalline polymer. Phys Rev Lett 90:098304. https://doi.org/10.1103/PhysRevLett.90.098304

Hegde M, Yang L, Vita F, Fox RJ, Watering RVD, Norder B, Lafont U, Francescangeli O, Madsen LA, Picken SJ, Samulski ET, Dingemans TJ (2020) Strong graphene oxide nanocomposites from aqueous hybrid liquid crystals Nat Commun 11. https://doi.org/10.1038/s41467-020-14618-0

Hongladarom K, Burghardt WR (1998) Molecular orientation, "region I" shear thinning and the cholesteric phase in aqueous hydroxypropylcellulose under shear. Rheol Acta 37:46–53

Huang G-R, Wang Y, Do C, Shinohara Y, Egami T, Porcar L, Liu Y, Chen W-R (2019) Orientational distribution function of aligned elongated molecules and particulates determined from their scattering signature. ACS Macro Lett 8:1257–1262. https://doi.org/10.1021/acsmacrolett.9b00496

Ilavsky J (2012) Nika: software for two-dimensional data reduction. J Appl Crystallogr 45:324–328. https://doi.org/10.1107/s0021889812004037

Jones G, Fornwalt HJ (1936) The viscosity of deuterium oxide and its mixtures with water at 25°C. J Chem Phys 4:30–33. https://doi.org/10.1063/1.1749743

Keates P, Mitchell GR, Pauvrel-Disdier E, Navard P (1993) In situ X-ray scattering study of anisotropic solutions of hydroxypropylcellulose subjected to shear flow. Polymer 34:1316–1319

Kiss G, Porter RS (1978) Rheology of concentrated solutions of poly(y-benzyl-glutamate). J Polym Sci Polym Symp 65:193–211

Kiss G, Porter RS (1980) Rheology of concentrated solutions of helical polypeptides. J Polymer Sci Phys 18:361–388

Kulicke WM, Kiss G, Porter RS (1977) Inertial normal-force corrections in rotational rheometry. Rheol Acta 16:568–572

Lang C, Kohlbrecher J, Porcar L, Radulescu A, Sellinghoff K, Dhont JKG, Lettinga MP (2019) Microstructural understanding of the length- and stiffness-dependent shear thinning in semidilute colloidal rods. Macromolecules 52:9604–9612. https://doi.org/10.1021/acs.macromol.9b01592

Larson RG (1990) Arrested tumbling in shearing flows of liquid-crystal polymers. Macromolecules 23:3983–3992. https://doi.org/10.1021/ma00219a020

Larson RG (1996) On the relative magnitudes of viscous, elastic and texture stresses in liquid crystalline PBG solutions. Rheol Acta 35:150–159

Larson RG, Doi M (1991) Mesoscopic domain theory for textured liquid crystalline polymers. J Rheol 35:539–563. https://doi.org/10.1122/1.550180

Lettinga MP, Dhont JKG (2004) Non-equilibrium phase behaviour of rod-like viruses under shear flow. J Phys Condens Matter 16:S3929–S3939. https://doi.org/10.1088/0953-8984/16/38/011

Lettinga MP, Dogic Z, Wang H, Vermant J (2005) Flow behavior of colloidal rodlike viruses in the nematic phase. Langmuir 21:8048–8057

Lopez CG, Rogers SE, Colby RH, Graham P, Cabral JT (2015) Structure of sodium carboxymethyl cellulose aqueous solutions: a SANS and rheology study. J Polym Sci B Polym Phys 53:492–501. https://doi.org/10.1002/polb.23657

Lopez CG, Colby RH, Cabral JT (2018) Electrostatic and hydrophobic interactions in NaCMC aqueous solutions: effect of degree of substitution. Macromolecules 51:3165–3175. https://doi.org/10.1021/acs.macromol.8b00178

López-Barrón CR, Wagner NJ (2011) Solvent isotope effect on the microstructure and rheology of cationic worm-like micelles near the isotropic-nematic transition. Soft Matter 7:10856–10863. https://doi.org/10.1039/c1sm05878a

Maffettone PL, Marrucci G, Mortier M, Moldenaers P, Mewis J (1994) Dynamic characterization of liquid crystalline polymers under flow-aligning shear conditions. J Chem Phys 100:7736–7743. https://doi.org/10.1063/1.466816

Marrucci G (1985) Rheology of liquid crystalline polymers. Pure Appl Chem 57:1545–1552

Marrucci G, Maffettone PL (1989) Description of the liquid-crystalline phase of rodlike polymers at high shear rates. Macromolecules 22:4076–4082

Mewis J, Mortier M, Vermant J, Moldenaers P (1997) Experimental evidence for the existence of a wagging regime in polymeric liquid crystals. Macromolecules 30:1323–1328

Moldenaers P, Mewis J (1986) Transient behavior of liquid crystalline solutions of poly(benzylglutamate). J Rheol 30:567–584. https://doi.org/10.1122/1.549861

Moldenaers P, Fuller G, Mewis J (1989) Mechanical and optical rheometry of polymer liquid-crystal domain structure. Macromolecules 22:960–965

Moldenaers P, Mortier M, Mewis J (1994) Transient normal stresses in lyotropic liquid crystalline polymers. Chem Eng Sci 49:699–707

Noel C, Navard P (1991) Liquid crystal polymers. Prog Polym Sci 16:55–110

Onogi S., Asada T. (1980) Rheology and rheo-optics of polymer liquid crystals

Picken SJ (1989) Clearing temperatures of aramid solutions in sulfuric acid. Macromolecules 22:1766–1771

Picken SJ, Aerts J, Visser R, Northolt MG (1990) Structure and rheology of aramid solutions- X-ray scattering measurements. Macromolecules 23:3849–3854

Picken SJ, Zwaag SVD, Northolt MG (1992) Molecular and macroscopic orientational order in aramid solutions- a model to explain the influence of some spinning parameters on the modulus of aramid yarns. Polymer 33:2998–3006

Picken SJ, Noirez L, Luckhurst GR (1998) Molecular conformation of a polyaramid in nematic solution from small angle neutron scattering and comparison with theory. J Chem Phys 109:7612–7617. https://doi.org/10.1063/1.477382

Sarkar N, Kershner D (1996) Rigid rod water-soluble polymers. J Appl Polym Sci 62:393–408

Ugaz VM, Cinader DK, Burghardt WR (1997) Origins of region I shear thinning in model lyotropic liquid crystalline polymers. Macromolecules 30:1527–1530

Viale S, Best AS, Mendes E, Jager WF, Picken SJ (2004a) A supramolecular nematic phase in sulfonated polyaramides. Chem Commun 14:1596–1597. https://doi.org/10.1039/b404809c

Viale S, Mendes E, Picken S, Santin O (2004b) Water soluble rigid rod polymers: a SANS study of shear-induced alignment and relaxation. Mol Cryst Liq Cryst 411:525–535. https://doi.org/10.1080/15421400490436449

Viale S, Best AS, Mendes E, Picken SJ (2005) Formation of aqueous molecular nematic liquid crystal phase in poly(p-sulfophenylene sulfoterephthalamide). Chem Commun:1528–1530. https://doi.org/10.1039/b416723f

Vroege GJ, Lekkerkerker HNW (1992) Phase transitions in lyotropic colloidal and polymer liquid crystals. Rep Prog Phys 55:1241–1309

Walker LM, Wagner NJ (1996) SANS analysis of the molecular order in poly(g-benzyl L-glutamate):deuterated dimethylformamide (PBLG:

d-DMF) under shear and during relaxation. Macromolecules 29: 2298–2301

Walker LM, Wagner NJ, Larson RG, Mirau PA, Moldenaers P (1995) The rheology of highly concentrated PBLG solutions. J Rheol 39: 925–952. https://doi.org/10.1122/1.550624

Walker LM, Kernick WA, Wagner NJ (1997) In situ analysis of the defect texture in liquid crystal polymer solutions under shear. Macromolecules 30:508–514

Wang Y, Gao J, Dingemans TJ, Madsen LA (2014) Molecular alignment and ion transport in rigid rod polyelectrolyte solutions. Macromolecules 47:2984–2992. https://doi.org/10.1021/ma500364t

Wang Y, Chen Y, Gao J, Yoon HG, Jin L, Forsyth M, Dingemans TJ, Madsen LA (2016) Highly conductive and thermally stable ion gels with tunable anisotropy and modulus. Adv Mater 28:2571–2578. https://doi.org/10.1002/adma.201505183

Wang Y, He Y, Yu Z, Gao J, Ten Brinck S, Slebodnick C, Fahs GB, Zanelotti CJ, Hegde M, Moore RB, Ensing B, Dingemans TJ, Qiao R, Madsen LA (2019) Double helical conformation and extreme rigidity in a rodlike polyelectrolyte. Nat Commun 10:801. https://doi.org/10.1038/s41467-019-08756-3

Wissbrun KF (1981) Rheology of rod-like polymers in the liquid crystalline state. J Rheol 25:619–662. https://doi.org/10.1122/1.549634

Wu ZL, Kurokawa T, Liang S, Gong JP (2010) Dual network formation in polyelectrolyte hydrogel via viscoelastic phase separation: role of ionic strength and polymerization kinetics. Macromolecules 43: 8202–8208. https://doi.org/10.1021/ma101558j

Yu Z, He Y, Wang Y, Madsen LA, Qiao R (2017) Molecular structure and dynamics of ionic liquids in a rigid-rod polyanion-based ion gel. Langmuir 33:322–331. https://doi.org/10.1021/acs.langmuir.6b03798